| 1 | Characteristics of Electron Precipitation Directly Driven |
|----------------|--|
| 2 | by Poloidal ULF waves |
| 3 | |
| 4 5 | Ze-Fan Yin ^{1,2} , Xu-Zhi Zhou ¹ , Wen Li ³ , Xiao-Chen Shen ³ , Robert Rankin ⁴ , Ji Liu ⁴ , Ze-Jun Hu ² , Jian-Jun Liu ² , Qiu-Gang Zong ¹ , Li Li ¹ , and Yong-Fu Wang ¹ |
| 6 | |
| 7 | ¹ School of Earth and Space Sciences, Peking University, Beijing 100871, China |
| 8 9 | ² MNR Key Laboratory for Polar Science, Polar Research Institute of China, Shanghai 200136, China |
| 10 | ³ Center for Space Physics, Boston University, Boston, MA 02215, USA |
| 11 | ⁴ Department of Physics, University of Alberta, Edmonton, AB T6G 2E1, Canada |
| 12 | |
| 13 | Corresponding authors: |
| 14 | Xu-Zhi Zhou (xzzhou@pku.edu.cn) and Wen Li (wenli77@bu.edu) |
| 15 | |
| 16 | Key Points: |
| 17 18 | • We investigate electron precipitation driven by poloidal-mode ULF waves that perturb the electron dynamics over bounce and drift timescales |
| 19 20 | • Precipitation occurs when electrons encounter westward electric fields, which enhance their cross-field energy and reduce the mirror heights |
| 21 22 23 | • Drift-resonant electrons can continuously encounter westward electric fields to have longer precipitation duration than non-resonant ones |

Abstract

A mechanism recently proposed for magnetospheric electron loss into the atmosphere is the precipitation directly driven by ultralow-frequency (ULF) waves. In this study, we quantitatively analyze the properties of ULF wave-induced precipitation by simulating the electron bounce and drift motion in poloidal-mode waves excited in a dipole magnetic field. Our results reveal that precipitation occurs only when electrons encounter a westward-directed wave electric field in the magnetosphere, which leads to cross-field energy enhancements and reduces their mirror heights. The simulations also demonstrate longer duration electron precipitation at the drift-resonance energy. We calculate the temporal variations of the energy spectrum for precipitating electrons and the total precipitating energy fluxes. These results improve our understanding of ULF wave-induced electron precipitation as well as provide a point of comparison for observations from balloons or ground-based instruments.

Plain Language Summary

Electron precipitation into the atmosphere is a major mechanism for electron loss in the radiation belts. A critical driver for the precipitation is the pitch-angle scattering induced by various plasma waves in the frequency range between several hertz and tens of kilohertz. On the other hand, ultralow-frequency (ULF) waves on the order of several millihertz are usually believed to play an indirect role, by modulating other types of waves. Here, we investigate a recently-proposed mechanism of electron precipitation directly driven by ULF waves, by simulating electron motion within a poloidal-mode wave field. The simulations, which cover electron bounce and drift time scales, reveal the important role of the azimuthal wave electric field in the induced electron precipitation. The precipitation occurs when the electrons encounter a westwarddirected electric field, which accelerates the electrons and reduces their mirror heights. The induced precipitation also shows an energy dependence; electrons at the driftresonance energy, which encounter a sustained westward-directed electric field, would have longer precipitation duration than non-resonant electrons. We further calculate the energy spectrum and the total fluxes of the precipitating electrons directly driven by ULF waves, and demonstrate that the effect could be potentially comparable to that caused by other magnetospheric waves.

1 Introduction

55

The loss of energetic electrons in the radiation belts, an important process of the 56 magnetospheric dynamics, is attributed to two mechanisms. The first mechanism is 57 magnetopause shadowing, which occurs when the electron drift paths intersect the 58 magnetopause (Hudson et al., 2014; Shprits et al., 2006; Ukhorskiy et al., 2006). The 59 other is the precipitation of energetic electrons into the atmosphere, which can be driven 60 effectively by resonant wave-particle interactions (W. Li et al., 2007; Millan & Thorne, 61 2007; Rodger et al., 2010). Many studies have shown that whistler-mode chorus waves 62 contribute significantly to electron precipitation by pitch-angle scattering (Horne & 63 Thorne, 2003; W. Li et al., 2014; Shprits et al., 2007), which also leads to the generation 64 of diffuse (Ni et al., 2008; Thorne et al., 2010) and pulsating aurorae (e.g., Nishimura 65 et al., 2010). Whistler-mode hiss, primarily confined to the plasmasphere and 66 plasmaspheric plumes, is another source for the resonant scattering of electrons in a 67 wide energy range (W. Li et al., 2019; Meredith et al., 2007; Ni et al., 2013). In addition, 68 69 it has been shown that Electromagnetic Ion Cyclotron (EMIC) waves play an important role in precipitating relativistic electrons (Jordanova et al., 2008; Kitamura et al., 2018; 70 Omura et al., 2010; Thorne & Kennel, 1971; Usanova et al., 2014). 71

72

73

7475

76

77

78

79

80

81

82

83

84

85

86

87

88

Another important factor of driving radiation belt dynamics is ultralow-frequency (ULF) waves, especially those in the Pc4-5 ranges (from 2mHz to 22mHz), which can lead to energy exchange and radial transport of energetic electrons via wave-particle driftresonant interaction (Fei et al., 2006; Klimushkin et al., 2021; Mann et al., 2013; Mikhailova et al., 2022; Su et al., 2015; Zong et al., 2017). Typically, ULF waves are categorized into toroidal and poloidal branches (Hughes, 1994), although they are often coupled with each other (Lee & Lysak, 1989; Wright & Elsden, 2020). Toroidal-mode waves have radial electric field and azimuthal magnetic field perturbations, whereas poloidal-mode waves are characterized by azimuthal electric field and radial magnetic field oscillations, both of which are accompanied by a compressional component of magnetic perturbations parallel to the local magnetic field. Extensive studies have been carried out to understand the fast acceleration of electrons during their drift motion in the azimuthal direction, which coincides with the direction of the electric field carried by poloidal-mode waves to facilitate an efficient energy exchange (Claudepierre et al., 2013; Dai et al., 2015; Foster et al., 2015; Hao et al., 2017; Zhou et al., 2015; Zhou et al., 2016; Zong et al., 2011; Zong et al., 2009). According to Southwood and Kivelson

(1981, 1982), drift resonance occurs when $\Omega - m\omega_d = 0$, where Ω and ω_d are wave frequency and particle drift frequency, and m is the azimuthal wave number. Particles satisfying the resonant condition encounter a constant phase of the wave electric field and then experience a sustained energy excursion.

93 94

95

96

97

98 99

100

101

102

103

104

105106

107

108

109

110

111

112

113

114

115

116

117

118

119

120

89

90

91

92

However, quantitative estimates of how ULF waves affect the precipitation of energetic electrons have been very limited. Previous studies have suggested that ULF waves could lead to the precipitation of cold electrons (Kostarev et al., 2021; Rankin et al., 2021), and it is generally believed that for more energetic electrons, the ULF waves can only play an indirect role via modulation of whistler-mode chorus (Jaynes et al., 2015; L. Li et al., 2022; W. Li et al., 2011; Qin et al., 2021; Xia et al., 2016; Zhang, Chen, et al., 2019) and EMIC waves (Loto'aniu et al., 2009; Zhang, Mourenas, et al., 2019). Recently, motivated by the ULF-modulation pattern of the electron precipitation in balloon observations (Millan et al., 2002; Millan et al., 2007), it has been proposed that ULF waves may directly induce the precipitation of energetic electrons (Brito et al., 2015; Brito et al., 2012). According to their simulations, when an energetic electron outside the loss cone is transported radially inward by the ULF waves, the enhanced field strength increases its equatorial pitch angle due to the conservation of the first and the second adiabatic invariants, and also enlarges the equatorial loss cone. Since the increase rate of the pitch angle is lower than that of the loss cone in a dipole geomagnetic field (see Figure 10 of Brito et al., 2015), it would enable the electron precipitation into the atmosphere. Rae et al. (2018) further suggested that the size of the loss cone is determined not only by the dipole field but also by the compressional ULF wave field, which could modulate the loss cone and facilitate stronger precipitation when energetic electrons drift into the wave-active region. In these studies, however, the role of the realistic wave field in modulating the electron's equatorial pitch angle is not considered. To have a more accurate understanding of the electron precipitation directly driven by ULF waves, it is required to analyze the electron motion in the fields of the wave, which would also enable important questions to be answered, e.g., how deep do electrons penetrate into the loss cone? What are the observational characteristics of ULF wave-induced precipitation? How large are the fluxes of the precipitated electrons? How important are ULF waves in precipitating electrons compared to the very-low-frequency (VLF) and extremely-low-frequency (ELF) waves? In this study, we carry out test particle simulations based on a coupled poloidalcompressional ULF wave model to understand electron dynamics and precipitation characteristics within two different time scales (the electron bounce and drift scales). Before presenting the results, in the next section, we first introduce the adopted wave model and our approach for simulating the electron motion.

128

129

2 Methods

- We adopt a dipole coordinate system (μ, ν, ϕ) , in which $\mu = \frac{\cos \theta}{r^2}$ and $\nu = -\frac{\sin^2 \theta}{r}$
- are expressed in terms of spherical coordinates (r, θ, ϕ) . In this coordinate system, ν
- can also be expressed by $v = -\frac{1}{LR_E}$, where R_E is Earth's radius and L represents the
- L-shell value. Here, the positive $\hat{\boldsymbol{e}}_{\nu}$ direction is perpendicular to the dipole field line
- pointing outward. At any specific L shell (i.e., a fixed ν), μ increases with latitude,
- with the positive \hat{e}_{μ} direction pointing northward along the dipole field line. The
- positive \hat{e}_{ϕ} direction points azimuthally eastward. The Earth's background dipole
- field is then defined by

138
$$\boldsymbol{B_0} = \frac{B_E R_E}{r^3} \sqrt{1 + 3\cos^2\theta} \,\hat{\boldsymbol{e}}_{\mu} = \frac{B_E R_E}{L^3} \frac{\sqrt{1 + 3s^2}}{(1 - s^2)^3} \hat{\boldsymbol{e}}_{\mu}, \tag{1}$$

where B_E is the equatorial magnetic field strength at Earth's surface, and $s = \cos \theta$.

- The poloidal wave electric field used in our study is a solution to the linearized ideal
- magnetohydrodynamic wave equations with coupling to the toroidal mode neglected.
- To excite the wave, a monochromatic driver is applied, as described in previous works
- (Rankin et al., 1999; Rankin et al., 2005; Wang et al., 2018). The azimuthal electric
- 145 field E_{ϕ} , for an Alfvén speed profile varying as $v_A(s) = v_A^{eq}(1+3s^2)$ along the
- geomagnetic field, is given by,

147
$$\mathbf{E}_{\phi} = \frac{E_0 \omega_0^3 \gamma R_E}{h_{\phi} \Delta} \cos[f_N(s+s^3)] \left\{ \sin(\omega_0 t - m\phi) - e^{-\frac{\gamma t}{2}} \frac{\omega_N^2 + \omega_0^2}{2\omega_0 \Gamma} \sin(\Gamma t - m\phi) + \frac{\omega_N^2 - \omega_0^2}{\omega_0 \gamma} \left[\cos(\omega_0 t - m\phi) - e^{-\frac{\gamma t}{2}} \cos(\Gamma t - m\phi) \right] \right\} \hat{\mathbf{e}}_{\phi}$$
(2)

- where v_A^{eq} is the Alfvén speed at the equatorial plane, $h_{\phi} = \frac{1}{|\nabla \phi|}$ is the scale factor,
- 150 $f_N = \frac{\pi}{2(s_m + s_m^3)}$, $s_m = \sqrt{1 \frac{1}{L}}$ corresponds to the latitude of the magnetic footprint at
- Earth's ionosphere, m is the azimuthal wave number, and E_0 controls the wave
- amplitude. The field line resonance occurs around a narrow range of L-shell centered

on $L=L_R$ where the eigenfrequency $\omega_N(L)\sim\omega_0\frac{L_R}{L}$ matches the constant driver frequency ω_0 . The other parameters are $\Delta=(\omega_N^2-\omega_0^2)^2+\omega_0^2\gamma^2$ and $\Gamma=\sqrt{\omega_N^2-\frac{\gamma^2}{4}}$, with γ defining the ionospheric damping rate of the waves. The wave magnetic field components, i.e., the parallel (compressional) component B_μ and radial component B_ν , are obtained from the Faraday's law. In this study, we set the field line resonance occurrence at geostationary orbit ($L_R=6.6$), and the wave period is set to be 120 seconds, i.e., $\omega_0=\frac{2\pi}{120}$. The other parameters are $E_0=5\text{mV/m}$, m=100, $\gamma=0.1\omega_0$. We show in Figure 1 profiles of the wave field, which demonstrates the characteristics of the narrowing coverage on L-shell and amplitude growth around the resonant field line.

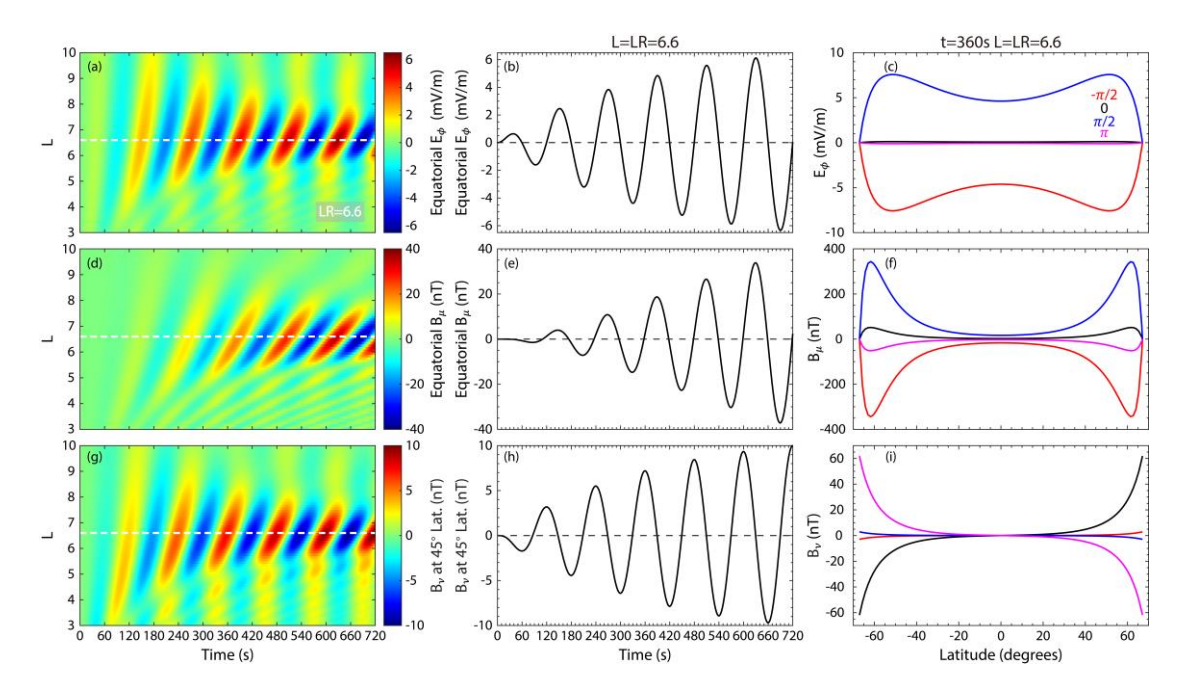


Figure 1. Overview of the coupled poloidal-compressional ULF wave field. The first row shows (a) the time-L shell variations of the equatorial azimuthal electric field; (b) the temporal variations of the equatorial azimuthal electric field at L = 6.6 where the field line resonance occurs, corresponding to the horizontal white dashed line in panel (a); (c) the latitude profile of the azimuthal electric field at L = 6.6 and t = 360s, with different colors corresponding to different wave phases. The following two rows, panels (d)-(f) and (g)-(i), are in the same format as the first row, except that they apply to the equatorial compressional magnetic field components and the radial magnetic field components at 45° latitude, respectively.

To examine electron precipitation directly driven by poloidal-mode ULF waves, we next conduct guiding-center (Northrop, 1963) test-particle simulations to investigate the electron dynamics in the wave field. In our simulations, a solid precipitation boundary at 100km altitude is assumed, which means that electrons below 100km are lost into the atmosphere. It is noteworthy that this assumption is a simplification of a rather complex loss process that involves the energy deposition and angular scattering of incident electrons and the dynamical and chemical changes of the upper and middle atmosphere (e.g., Randall et al., 2007; Sinnhuber & Funke, 2020). A more accurate assessment of the complex interaction process could change some of our conclusions (see discussions in Section 5). However, the inclusion of the complex interaction process requires complicated simulations (Fang et al., 2010; Lehtinen et al., 1999; Marshall & Bortnik, 2018; Xu et al., 2018) and thus will be left for a future study.

3 Electron Motion within Bounce Time Scale

We first study the electron motion within a half bounce period. The precipitation of an electron in our model indicates that it is the first time the electron reaches the 100km altitude, or equivalently, the electron's mirror point (say, in the northern hemisphere) must have just moved to below 100km during its final half-period of bounce motion from its mirror point above 100km in the southern hemisphere. Therefore, a series of critical electrons are launched at 100km altitude in the southern hemisphere with 90° pitch angle, and their trajectories within a half bounce period under the influence of the ULF wave field would provide important information on the angular size of the precipitating electrons.

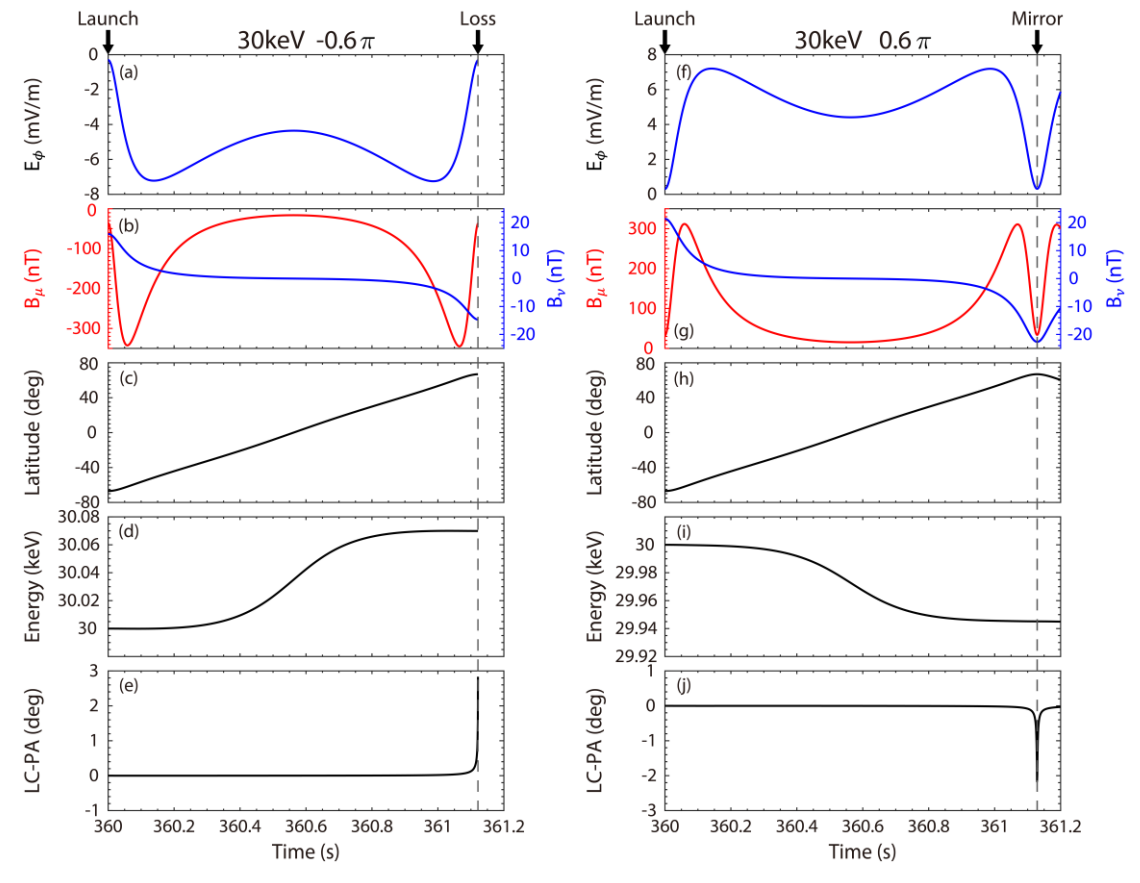


Figure 2. Overview of the variations during the electron bounce time scale. The left panels show the temporal variations of (a) the azimuthal electric field, (b) the compressional (red) and radial (blue) magnetic components of the ULF wave field, (c) latitude, (d) kinetic energy, and (e) the difference of the local loss cone and pitch angle (LC-PA) along the electron's bounce trajectory from its launch point at 100km altitude in the southern hemisphere. The launched electron has an initial energy of 30keV and the initial phase in the wave field of -0.6π . The right panels, (f)-(j), are in the same format as the left panels, except that the initial phase of the launched electron in the wave field is 0.6π . The vertical dashed lines mark the time when the electron encounters the precipitation boundary (left) or mirrors back (right) in the northern hemisphere, respectively.

Figure 2 shows the bounce motion of two typical electrons launched at $L=L_R=6.6$ and t=360s, during which the equatorial amplitude of the wave electric field is about 5mV/m. The two test electrons have the same initial kinetic energy 30keV but different azimuthal locations to have different phases ζ in the wave field (where $\zeta=\omega_0 t-m\phi$). The electron with $\zeta=-0.6\pi$ encounters a westward-directed electric field (see

Figure 2a), a southward wave magnetic field (the compressional component, see the red line in Figure 2b), and a radial magnetic field that reverses direction across the equator (the blue line in Figure 2b) during its bounce motion towards the northern hemisphere (see the latitude variations in Figure 2c). The electron's energy variation, given in Figure 2d, indicates its acceleration during this time interval. Given the shorter time scale of the electron's bounce motion (~1s) than the wave period (120s), the variations of the wave field shown in Figure 2 are mainly caused by spatial rather than temporal effects.

To understand the role of the ULF wave field in the electron pitch angle scattering, we next derive the local bounce loss cone based on the local magnetic field strength and that of the precipitation boundary at 100km, and calculate the difference between the local loss cone and pitch angle (LC-PA) to delineate their relative variations. The LC-PA values greater than zero indicate that the electron would fall into the loss cone. As shown in Figure 2e, the LC-PA value increases from zero at the launch point to \sim 3° when the electron reaches the precipitation boundary in the northern hemisphere. In other words, the electron pitch angle is \sim 87° when it precipitates into the atmosphere.

This relative variation of the loss cone and pitch angle can be understood from the conservation of the first adiabatic invariant $\mu_{ad} = p_\perp^2/(2m_eB)$, where p_\perp is the local perpendicular momentum, m_e is the electron mass and B is the local magnetic field strength. Since the ULF wave period is much longer than the electron gyro-period (<1ms), the first adiabatic invariant is conserved during the electron bounce motion. Under the effect of the westward-directed electric field, the electron would move inward and be located at a lower L-shell when it approaches the precipitation boundary. Given the same altitude of the electron's launch point and the precipitation boundary at 100km, the magnetic field strength at the precipitation boundary will be smaller than that at the launch point (with a relative difference less than 10^{-4}), indicating a smaller perpendicular energy of the electron at the precipitation boundary. Meanwhile, the electron's energy is enhanced (Figure 2d; with a relative change greater than 10^{-3}). The lower perpendicular energy and higher total energy indicate a finite parallel momentum at the precipitation boundary, which in turn causes the reduced pitch angle and therefore a LC-PA value greater than zero. In other words, it is the ULF-wave

induced acceleration that indicates a larger magnetic field strength (or equivalently, an altitude lower than 100km) at the electron's mirror point.

In contrast, the electron with the phase $\zeta = 0.6\pi$ in the wave field would encounter the eastward-directed electric field (see Figure 2f) and be decelerated (Figure 2i). As one would expect based on the μ_{ad} conservation, the decelerated electron would bounce back at an altitude above 100km (see the vertical dashed line in Figures 2f-2j), with the LC-PA value less than zero at the mirror point (see Figure 2j).

We next investigate the initial energy- and phase-dependence of the electron characteristics, to better understand the role of the ULF wave-induced acceleration in the electron precipitation. To do so, we apply the same test-particle tracing procedure to a series of electrons, launched at an altitude of 100km in the southern hemisphere with different energy and phase ζ . Then we examine the electron energy changes and the LC-PA values when they reach the precipitation boundary (for those electrons lost into the atmosphere) or their respective mirror points (for those bouncing back at altitudes above 100km) in the northern hemisphere. The resulting energy changes and the LC-PA values are shown in Figures 3a and 3b, respectively, as functions of initial phase ζ and energy E_k .

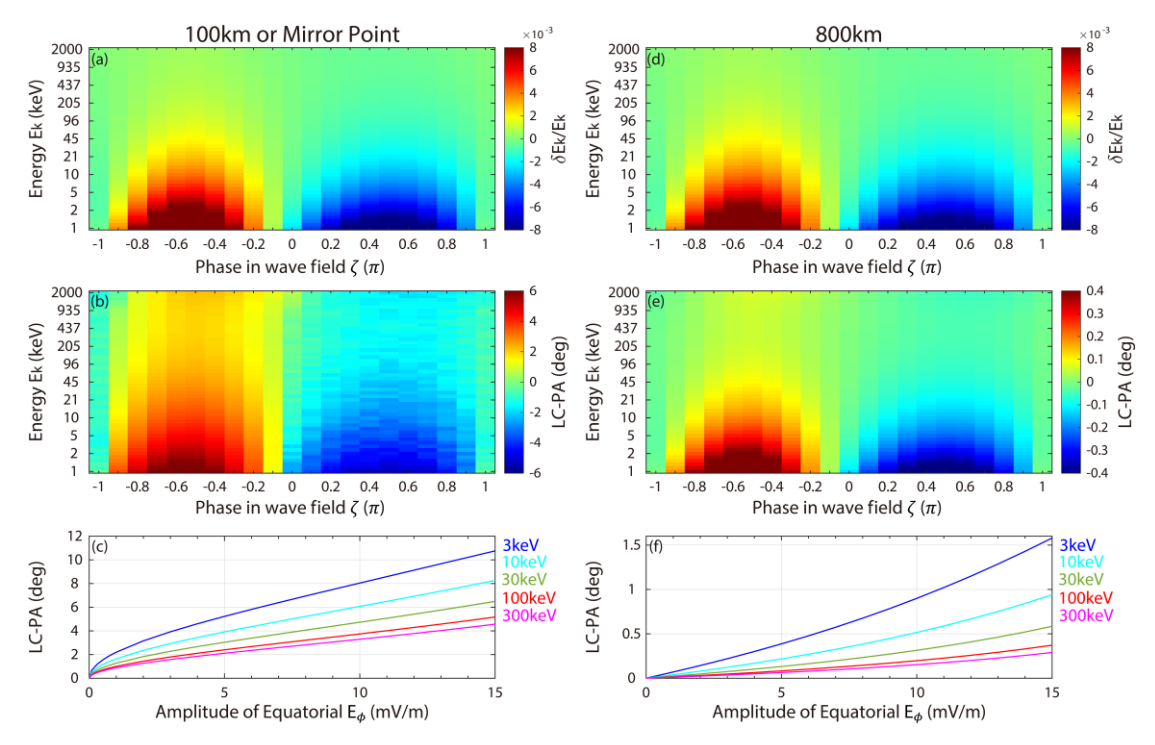


Figure 3. Overview of the ULF wave-induced variations within the electron bounce time scale under different conditions. The left panels show (a) the relative energy changes and (b) the LC-PA values at 100km altitude (if precipitation occurs) or at the mirror point, for electrons with different energies and phases in the wave field; (c) the variations of the maximum LC-PA value as functions of the electric field amplitude, in which different colors correspond to different electron energies. The right panels, (d)-(f), are in the same format as the left panels, except that they show the relevant quantities at 800km altitude.

Obviously, electrons encountering a westward-directed electric field (with the initial phase in the wave field between $-\pi$ and 0) are accelerated (with relative energy change $\delta E_k/E_k>0$, see Figure 3a) and then precipitated into the atmosphere (with LC-PA>0, see Figure 3b). In contrast, electrons in an eastward-directed electric field (with the initial phase ζ between 0 and π) are decelerated ($\delta E_k/E_k<0$, see Figure 3a) and bounce back (LC-PA<0, see Figure 3b) at mirror points above 100km. These results, consistent with the expectations based on μ_{ad} conservation, also reveal the energy- and wave amplitude-dependence of the ULF wave-induced precipitation within the bounce time scale. The relative energy enhancements, given in Figure 3a, tend to be larger for lower-energy electrons within larger westward-directed electric fields (with ζ closer to $-\pi/2$), which leads to stronger precipitation (larger LC-PA values,

see Figure 3b). Such a dependence on electron energy can be understood from the fact that the electron drift speed is proportional to its energy E_k , whereas its bounce period is proportional to $1/\sqrt{E_k}$ (Hamlin et al., 1961). In other words, the absolute and relative energy changes caused by a given electric field must be proportional to $\sqrt{E_k}$ and $1/\sqrt{E_k}$, respectively, within a half bounce cycle. Figure 3c further shows the maximum LC-PA value as a function of the amplitude of the equatorial electric field, in which different colors correspond to electrons with different energies. The results indicate that electrons penetrate deeper into the loss cone under larger electric fields, with a $\sim 10^{\circ}$ pitch angle variation for electrons of a few keV under strong electric field $\sim 15 \, \mathrm{mV/m}$.

To facilitate a potential comparison with spacecraft measurements, we show in Figures 3d-3f the energy and LC-PA changes before the electrons reach a virtual spacecraft at 800km altitude in the northern hemisphere (since most spacecraft measuring particle precipitation, like the POES satellites, follow polar or sun-synchronous orbits). The resulting trends are very similar to those at 100km or at the mirror points (Figures 3a-3c), except that the LC-PA changes are much lower at 800km. For example, the maximum LC-PA value at 800km is ~1.5° (in comparison with ~10° at 100km) under strong equatorial electric field ~15mV/m. The significant differences between the LC-PA values at 100km and 800km (compare Figures 3b-3c and 3e-3f) result from the dipole field configuration. Based on the magnetic field strength at 100km and 800km altitude at L=6.6, the local loss cone at 800km is about 59°. Considering an electron within the loss cone, with a pitch angle of 80° at 100km, the conservation of the first adiabatic invariant requires its pitch angle to be ~57.5° at 800km, which corresponds to the reduced LC-PA value of ~1.5°.

The minor pitch-angle extent of the precipitating electrons inside the loss cone indicates the difficulty of identifying them in spacecraft observations at 800km. For example, the Space Environment Monitor (SEM-2) instrument (Evans & Greer, 2004) onboard POES, widely used in the study of particle precipitation (e.g., Capannolo et al., 2019; Carson et al., 2013; W. Li et al., 2013; W. Li et al., 2019), could measure electron flux inside the loss cone with a 0° telescope oriented towards local zenith. However, the upper edge of the pitch-angle coverage of this 15°-wide telescope is about 35° at high latitude (Rodger et al., 2010), which means it could only measure the electron flux

relatively deep inside the loss cone (with a local loss cone of ~59°). Therefore, the POES observations may not be suitable for investigation of the electron precipitation directly driven by ULF waves. The more recent ELFIN CubeSats (Angelopoulos et al., 2020), although having more advanced pitch-angle observation capabilities with full pitch-angle coverage and the resolution of ~22.5°, would still be difficult to identify the minor pitch-angle extent of the precipitating electrons induced by the ULF waves. The finer observations for the pitch-angle distributions near the loss cone are required for satellite measurements to identify these electrons. The balloons or ground-based observations could be more suitable ways, since they usually exhibit a summed effect over the pitch-angle ranges. In the next section, we will utilize the backward-tracing approach to simulate the temporal variations of the electron precipitation during a longer period (the electron drift time scale), which could enable a potential comparison to real observations.

4 Electron Motion within Drift Time Scale

To investigate the variations of the ULF wave-induced electron precipitation within their drift time scale, we set a virtual observer at 100km altitude in the northern hemisphere (with fixed magnetic longitude $\phi=0$ and L-shell L=6.6), and trace the electrons with different energies and pitch angles from the virtual observer backward in time to t=0 when there is no wave activity. The wave parameters adopted are the same as in Section 2, which corresponds to the drift-resonance energy of ~50keV. In other words, the ~50-keV electrons would experience negligible phase variations in the wave field, and be accelerated continuously (for those with ζ between $-\pi$ and 0) to provide a sustained source for electron precipitation. Therefore, we show in Figure 4 a comparison between the trajectories of two sample electrons, a non-resonant and a resonant electron, before their precipitation into the atmosphere.

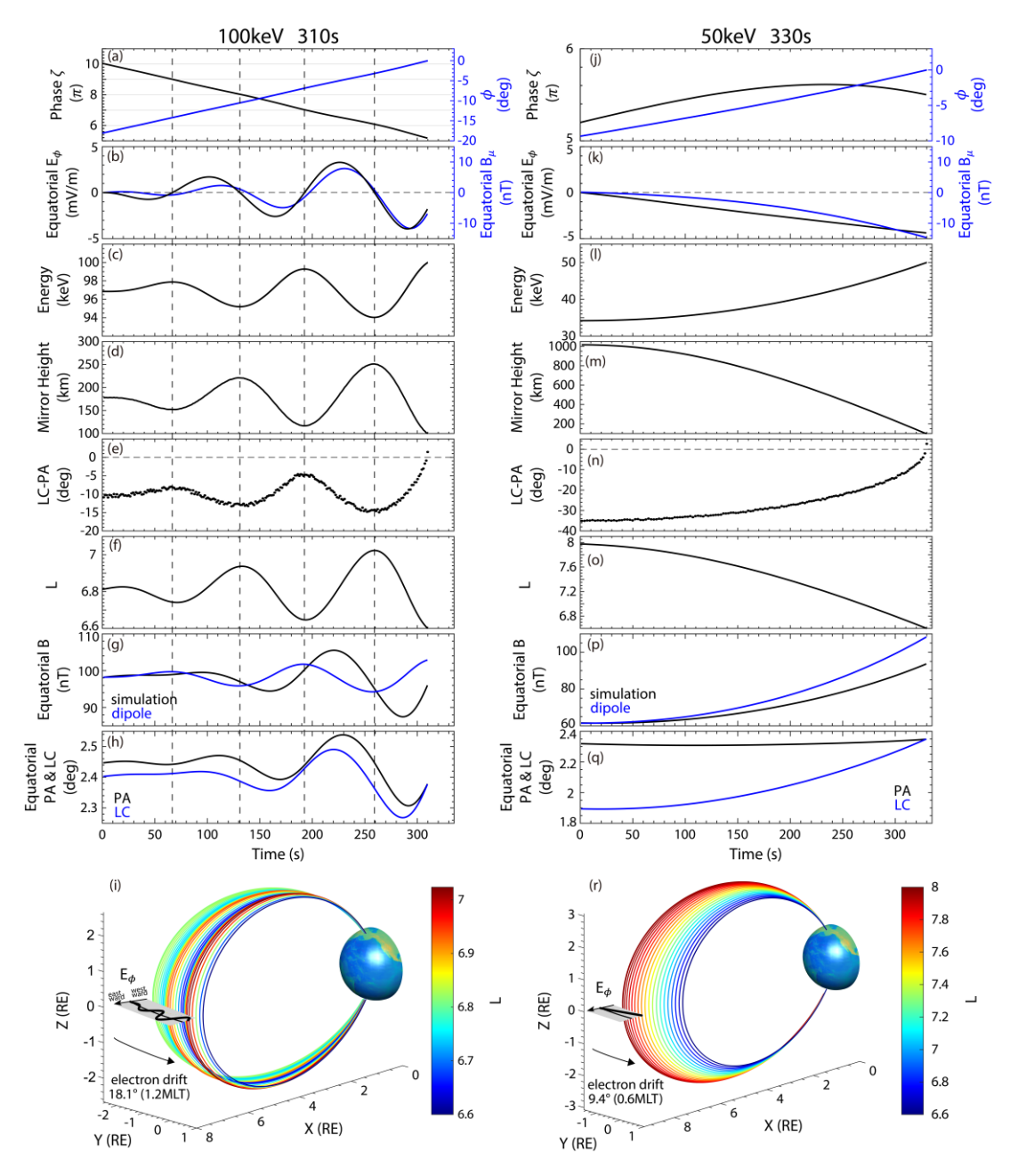


Figure 4. Variations of the simulated electrons within the drift time scale. The left panels show the temporal variations of the 100-keV electron precipitating at 310s, including (a) the electron's phase in the wave field (black) and its azimuthal location (blue), (b) the encountered equatorial azimuthal electric field (black) and compressional magnetic field (blue), (c) the electron's energy, (d) the altitude of the mirror points in the northern hemisphere, (e) the difference between the local loss cone and the electron's pitch angle at the mirror points, (f) the L-shell value, (g) the encountered equatorial magnetic field strength (black) and the background dipole field strength (blue), and (h) the equatorial pitch angle (black) and loss cone (blue). The vertical

dashed lines mark the time when the encountered azimuthal electric field is equal to zero. (i) Three-dimensional motion of the electron's guiding-center, in which different colors represent the different L-shell values. The value of the encountered equatorial azimuthal electric field is also shown as the black curve in the inserted plot, which is the same as the black line in panel (b). The right panels, (j)-(r), are in the same format as the left panels, except that they apply for the 50-keV electron (around the drift-resonance energy) precipitating at 330s.

The left panels in Figure 4 correspond to an electron that precipitates at t=310s with an energy of 100keV, which is higher than the drift-resonance energy. The electron's phase in the ULF wave field keeps decreasing during its eastward drift around the Earth (see Figure 4a), which indicates that the electron must encounter an oscillating electric field (see the black line in Figure 4b for the equatorial azimuthal electric field). When the electric field is in a westward direction, the electron would be accelerated (see Figure 4c) to reduce the mirror height (see Figure 4d) and cause an inward motion (see Figure 4f). A reversed trend could also be observed during the time interval of eastward-directed electric field (see the trend reversal at each vertical dashed line in Figures 4a-4f). This electron eventually reaches the precipitation boundary at 100km altitude, with the LC-PA value greater than zero (see Figure 4e). Figure 4i illustrates the electron's bounce and drift trajectory during the entire 310s-interval, with the line color displaying the L-shell variations in association with the wave electric field encountered.

We also investigate the variations of the electron's equatorial pitch angle and loss cone during its drift motion. Figure 4g shows the equatorial magnetic field strength (black line) encountered by the electron in comparison with the background dipole field (blue line). Figure 4h shows the variations of the equatorial pitch angle (black line) and loss cone (blue line). Consistent with the Rae et al. (2018) scenario, the modulation of the equatorial magnetic field strength by the compressional wave field affects the size of the equatorial loss cone (compare the variations of magnetic field strength in Figure 4g and loss cone in Figure 4h). However, the electron's equatorial pitch angle is not only modulated by the field strength variations, but also the energy variations driven by the wave electric field. As a result, the electron precipitation does not simply occur when the compressional magnetic field is in the northward direction (with enlarged loss cones, as predicted in Rae et al. (2018)). Moreover, the compressional wave field could also

change the variation trend of the magnetic field strength along the electron's radial motion (see the difference between dipole and total magnetic field in Figure 4g). The electron could even encounter a smaller equatorial magnetic field during its inward motion (e.g., compare variations from ~260s to ~280s in Figure 4f and 4g), leading to a reduction of the equatorial pitch angle (to satisfy the μ_{ad} conservation; see Figure 4h). This is inconsistent with the results based on the simple dipole field that the electron's pitch angle should be enlarged when it moves radially inward (Brito et al., 2015), which reveals the important but previously-overlooked role of the realistic wave field in modulating the electron's equatorial pitch angle.

On the other hand, the drift-resonant electron (see the right panels of Figure 4) would experience an electric field in a constant, westward direction (see the black line in Figure 4k) due to the relatively stable phase in the wave field (see Figure 4j). Therefore, the electron can be accelerated continuously (see Figure 4l), which in turn leads to the monotonic decrease of the mirror height (see Figure 4m) and the increase of the LC-PA value at the mirror point (see Figure 4n). The electron trajectory is also characterized by its inward motion (see its L-shell variations in Figure 4o) caused by the continuing westward-directed electric field (see Figure 4r). The continuous inward motion results in the increasing strength of the encountered equatorial magnetic field (see Figure 4p), which leads to the gradually enlarged equatorial loss cone (see the blue line in Figure 4q). On the other hand, the equatorial pitch angle experiences weaker variations (see the black line in Figure 4q) and eventually reaches the loss cone to cause the electron precipitation.

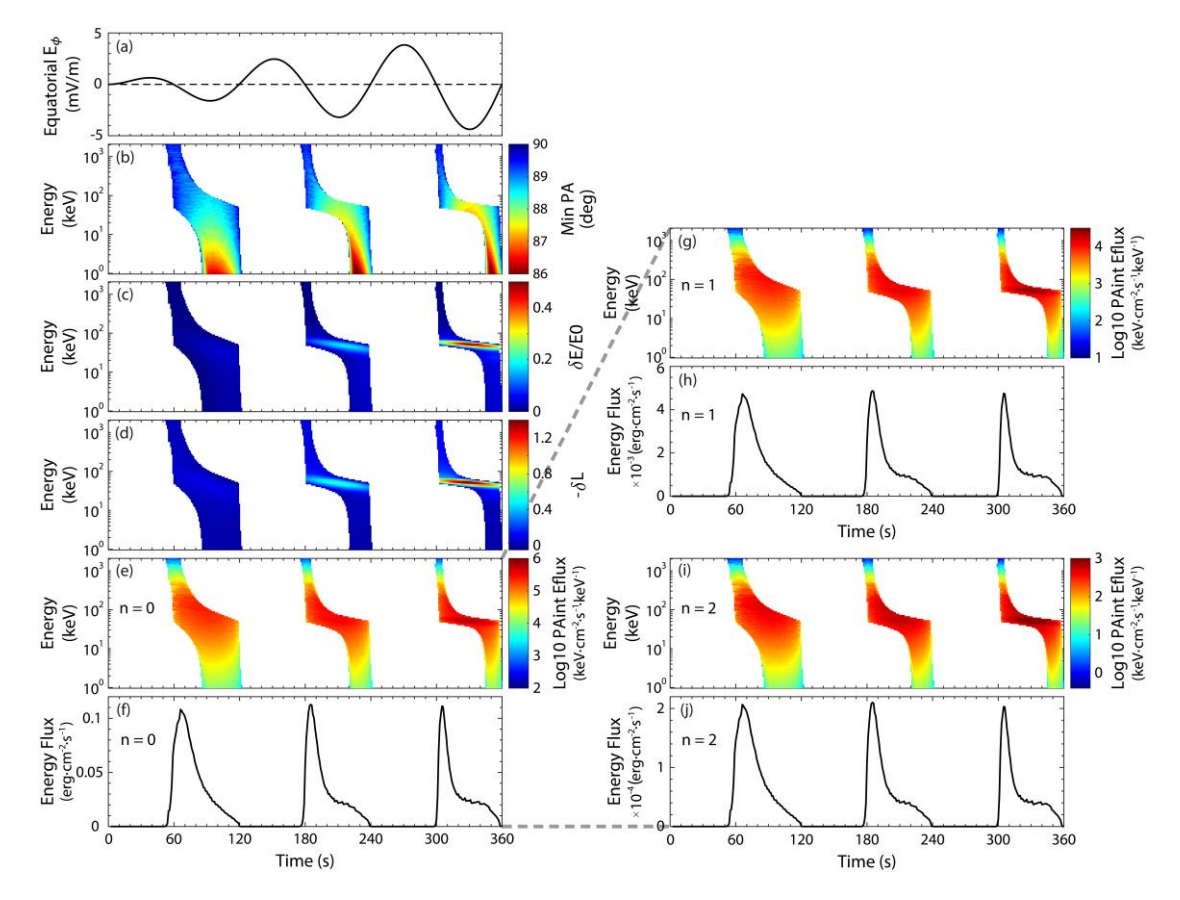


Figure 5. Simulated observations of a virtual observer at 100km altitude of L=6.6 with a fixed azimuthal location. (a) Temporal variations of the equatorial electric field at the same magnetic longitude as the virtual observer. The properties of the precipitated electrons include (b) the observed minimum pitch angle, (c) the relative energy changes, (d) the inward L-shell variations, (e) the energy flux integrated over pitch angle, and (f) the total precipitating energy flux, with the initial electron distributions prescribed to be isotropic (n=0 in equatorial phase space density distribution $f = f_{90} \sin^n \alpha$). The panels (g)-(h) and (i)-(j) are in the same format as the panels (e)-(f), expect that they apply for the initial distributions with n=1 and n=2, respectively.

To determine the fluxes of precipitated electrons as functions of energy and time, we next trace electrons of different energies and pitch angles within the loss cone from the virtual observer at 100km altitude backward in time to t=0 so that their initial properties could be obtained. Note that if an electron reaches the precipitation boundary during the backward tracing procedure, or if its pitch angle is smaller than the local loss cone at t=0, this electron would be considered absent (since it has been precipitated without having a chance to reach the virtual observer). For other electrons, their

associated phase space densities are determined based on Liouville's theorem with the initial equatorial distribution given by $f = f_{90} \sin^n \alpha$, in which the equatorial phase space density with 90° pitch angle (f_{90}) is given by AE8 model (Vette, 1991, which is extrapolated to energies lower than 50 keV) and n controls the distribution profile over the equatorial pitch angle (α) . Note that near the geostationary orbit, the MIN and MAX versions of the AE8 model are the same. The fluxes of the precipitated electrons at the virtual observer could thus be derived, which are shown in Figure 5.

It is shown that the electron precipitation directly driven by ULF waves mainly occurs during the interval of westward-directed electric field (compare the equatorial electric field at the same azimuthal location as the virtual observer in Figure 5a to the precipitated electron properties in Figures 5b-5f). This is consistent with the conclusion from the analysis on the bounce time scale that the electron must be accelerated during the final half bounce period before its precipitation. A minor exception occurs for higher-energy electrons, which could be precipitated in association with weak eastward-directed electric field (see Figure 5 for precipitated electrons near t = 60, 180, and 300s, at energies above 1MeV). This is because of the reversal in the electric field direction during the electron's final half bounce period, which in turn is caused by the rapid ζ variations due to their fast drift motion with respect to the ULF wave propagation. The minimum pitch angles of the precipitated electrons (Figure 5b) indicate that lower-energy electrons could penetrate deeper into the loss cone, a feature also displayed in Figure 3 within the bounce time scale. Moreover, the precipitated electrons have all been accelerated (see the relative energy changes in Figure 5c) and transported inward (see the L-shell changes in Figure 5d) by the ULF waves, further demonstrating the important role of the acceleration induced by the westward-directed wave electric field in the electron precipitation.

An interesting feature in our simulation is that the duration of electron precipitation varies with energy. At the drift-resonance energy (~50keV), the electron precipitation occupies nearly the entire time interval with westward-directed electric field, whereas the precipitation at higher and lower energies occurs within a narrower time range before and after the wave trough, respectively. The precipitation time range further shortens as the wave continues to grow (compare the three wave cycles in Figure 5). This is because the non-resonant electrons would experience positive and negative

energy excursions as they drift across different ζ phases. To precipitate at a specific time (and not during the previous cycle of ζ variations), the energy gain during the current cycle with westward-directed electric field (prior to the precipitation time) must exceed the energy loss within the entire half cycle with eastward-directed electric field. Therefore, the electron precipitation can only occur during the latter part of the positive energy excursions if the wave growth is not too significant. The resonant electrons, on the other hand, could undergo a sustained acceleration during their drift motion (see the example in Figure 4), which enables a continuous precipitation that occupies the entire time range with westward-directed electric field.

Figure 5e shows the energy spectrum of the pitch-angle integrated energy fluxes, which is determined based on the assumption that the initial electron distribution is isotropic (n=0) except for an emptied loss cone. Obviously, the electrons near the drift-resonance energy have larger differential energy fluxes due to their more efficient acceleration (see Figure 5c). The integrated energy fluxes for precipitated electrons, given in Figure 5f, indicate the periodic variations of the precipitating fluxes during periods of westward-directed electric field. Within each precipitation period, the integrated fluxes appear to decrease with time, which indicates that the majority of the fluxes are from electrons with higher energies (compare Figures 5e and 5f). Note that the peak fluxes, ~ 0.1 erg/cm² per second, largely depend on the assumption of electron initial distributions. In the case where the initial distribution has smaller fluxes near the equatorial loss cone, with n=1 (see Figures 5g and 5h) or n=2 (see Figures 5i-5j), the precipitating fluxes would be reduced by one or three orders of magnitude.

5 Discussion

This study focuses on the temporal variations of the electron precipitation directly driven by ULF waves, which provides a comparison point for potential observations from Low-Earth-Orbiting Satellites, balloons and ground-based instruments. To compare the simulation results to actual observations, the precipitated electron characteristics should be converted to observable quantities such as the X-ray counts for balloon measurements. Such a conversion procedure involves the interaction between precipitating electrons and atmospheric particles, which could be achieved by

more sophisticated Monte Carlo simulations in future studies (Berger & Seltzer, 1972; Foat et al., 1998; Millan et al., 2013).

510511

512

513

514

515

516

517

518519

520

521

522

523

524525

526

527

528

529

530

531

532

508

509

On the other hand, the simulation in this study provides a way to compare the electron precipitation driven by ULF waves and by other waves. The precipitating energy fluxes, which maximize at ~ 0.1 erg \cdot cm⁻² \cdot s⁻¹, are weaker than but still comparable to the precipitation induced by chorus waves during geomagnetic quiet periods (~0.3-2erg · $cm^{-2} \cdot s^{-1}$), although they are much weaker than those during geomagnetic disturbances ($\sim 3-10 \text{ erg} \cdot \text{cm}^{-2} \cdot \text{s}^{-1}$, see Ma et al., 2020; Ni et al., 2014). The characteristic energy of the chorus-induced precipitation is tens of keV, while higherenergy electrons contribute more to the energy fluxes of the ULF wave-induced precipitation. These precipitating energy fluxes are also comparable to those induced by hiss waves during disturbed conditions (~ 0.3 -1erg \cdot cm⁻² \cdot s⁻¹, Ma et al., 2021). Note that this comparison is rather inaccurate, since the simulation results largely depend on the electron distribution before the ULF wave occurrence, which could be enhanced significantly during geomagnetic storms and/or substorms (Kataoka & Miyoshi, 2006; McPherron, 1979; Yin et al., 2019). The enhanced source population could in turn lead to enlarged precipitation and therefore an enhanced ground-based response. Furthermore, the broadband characteristics of the ULF waves during geomagnetic disturbances would correspond to a wider drift-resonance energy range of the electrons (Murphy et al., 2020; Posch et al., 2003), which could allow more electrons to undergo longer-duration precipitation (as shown in Figure 5). These factors would strengthen the effect of ULF waves in the electron precipitation. Nevertheless, the relative role of electron precipitation directly driven by ULF waves and other magnetospheric waves needs further investigations.

533534

535

536

537

538

539

540

541

Moreover, it is worthy to note that the simulation results could also be affected by the ULF wave parameters. The enlargement of the wave amplitude, as shown in Figure 3c, would lead to a greater penetration of pitch angle into the loss cone within the last bounce of precipitated electrons, resulting in a larger total precipitating flux. The variations of the wave frequency and the azimuthal wave number, on the other hand, would have little effect on the electron bounce motion because of the short time scale. However, the wave frequency and the azimuthal wave number, together with the L-shell of the wave field, determines the drift-resonance energy of electrons at which the

longer precipitation duration would happen (as shown in Figure 5). A higher wave frequency, a smaller azimuthal number, and/or a smaller L-shell would lead to a higher drift-resonance energy. Considering the larger contribution of high-energy electrons in the total precipitating fluxes in Figure 5, a higher drift-resonance energy could lead to an enhanced profile of the total precipitating fluxes.

Although we only focus on poloidal-mode ULF waves in this study, the mechanism that ULF wave-induced electron acceleration could lower the mirror height to cause precipitation also applies to toroidal ULF waves. Toroidal ULF waves are usually considered less efficient in accelerating electron since the wave electric field is in the radial direction, or perpendicular to the electron drift paths. Nevertheless, it has been proposed that toroidal-mode ULF waves can also interact with the electrons via drift resonance if the asymmetry of the background magnetic field (Elkington et al., 1999) or the compressional wave magnetic field components (L. Li et al., 2021) are considered. Since poloidal and toroidal waves are usually coupled in the magnetosphere, it would be important to consider the electron acceleration and precipitation in a coupled wave field to obtain more realistic results, although it could be more complex than those in the single mode wave field. Future studies are needed to investigate the details of the electron precipitation in the coupled wave field.

Finally, it is important to note that the conclusions in this study are largely based on the assumption of a solid precipitation boundary at 100km altitude, whereas the actual loss process of the electrons in the atmosphere is more complex. The incident electrons with different energies and pitch angles would result in different atmospheric responses, which in turn lead to different energy deposition and backscatter extent (Marshall & Bortnik, 2018). The backscattered electrons would have mirror points below 100km, and their follow-up motion within the bounce time scale would correspond to a deeper penetration into the loss cone. For example, if we adopt the same parameters as in Figures 2a-2e, a backscattered 30-keV electron launched from 80km altitude in the southern hemisphere would have a LC-PA value of ~6° at 100km in the northern hemisphere (compare to ~3° in Figure 2e). The enlarged pitch-angle range would lead to a greater precipitating flux and indicate the possibility of measurements from low-earth-orbiting satellites. Moreover, the existence of the backscattered electrons would also relax the constraint that electron precipitation occurs during the interval of

westward-directed electric field. To take into account the complicated process of atmospheric collision, it is probably required to combine the test-particle simulation with sufficient electrons via the Monte Carlo approach, in which the information of energy deposition and backscattered population could be provided by the electron-atmosphere-interaction model (e.g., Lehtinen et al., 1999; Marshall & Bortnik, 2018). The simulation should provide more realistic characteristics of the ULF wave-induced precipitation, which will be addressed in a future study.

6 Summary

In this study, we utilize test-particle simulations in a coupled poloidal-compressional ULF wave model, to investigate the electron precipitation characteristics directly driven by ULF waves within the bounce and drift time scales. The main results are as follows:

(1) The electron precipitation directly driven by poloidal ULF waves is closely related to the azimuthal electric field. The precipitation usually occurs when the electrons encounter a westward-directed electric field, which leads to their acceleration and, consequently, a reduced mirror height.

(2) Electrons around the drift-resonance energy could encounter a stable phase in the wave field and thus experience a sustained acceleration under westward-directed electric field, which correspond to a longer duration of precipitation than non-resonant electrons.

(3) The ULF waves could only drive the precipitation of electrons near the loss cone. The lower-energy electrons could penetrate deeper into the loss cone, although the pitch angle variations are still less than 10 or 2 degrees at 100km or 800km altitudes even for low-energy, keV electrons. This is very hard to be observed in space.

(4) The ULF wave-induced precipitating energy flux could reach $\sim 0.1~{\rm erg\cdot cm^{-2}\cdot s^{-1}}$, which could lead to electron precipitation signals potentially observable by balloons or other ground-based instruments.

608 **Acknowledgements**

- This study has been supported by NSFC grants 42174184, 41974191. W. Li would like
- to acknowledge the Alfred P. Sloan Research Fellowship FG-2018-10936 and the NSF
- grant of AGS-2019950. R. Rankin is supported by grants from NSERC and the
- 612 Canadian Space Agency. J. Liu is supported by NSERC.

613

614

Data Availability Statements

- This study is a theoretical work without observational data. The simulation results and
- 616 the code to produce the figures in this manuscript are available at
- 617 https://doi.org/10.5281/zenodo.7576260.

619 **References**

- Angelopoulos, V., Tsai, E., Bingley, L., Shaffer, C., Turner, D. L., Runov, A., et al. (2020). The ELFIN
 Mission. Space Science Reviews, 216(5), 103. https://doi.org/10.1007/s11214-020-00721-7
- 622 Berger, M. J., & Seltzer, S. M. (1972). Bremsstrahlung in the atmosphere. *Journal of Atmospheric and*
- 623 Terrestrial Physics, 34(1), 85-108.
- https://www.sciencedirect.com/science/article/pii/0021916972900062
- Brito, T., Hudson, M. K., Kress, B., Paral, J., Halford, A., Millan, R., & Usanova, M. (2015). Simulation
- of ULF wave-modulated radiation belt electron precipitation during the 17 March 2013 storm.
- 627 Journal of Geophysical Research: Space Physics, 120(5), 3444-3461.
- 628 https://doi.org/10.1002/2014JA020838
- Brito, T., Woodger, L., Hudson, M., & Millan, R. (2012). Energetic radiation belt electron precipitation
- showing ULF modulation. Geophysical Research Letters, 39(22).
- https://doi.org/10.1029/2012GL053790
- 632 Capannolo, L., Li, W., Ma, Q., Shen, X. C., Zhang, X. J., Redmon, R. J., et al. (2019). Energetic Electron
- Precipitation: Multievent Analysis of Its Spatial Extent During EMIC Wave Activity. *Journal*
- 634 of Geophysical Research: Space Physics, 124(4), 2466-2483.
- 635 https://doi.org/10.1029/2018JA026291
- 636 Carson, B. R., Rodger, C. J., & Clilverd, M. A. (2013). POES satellite observations of EMIC-wave driven
- relativistic electron precipitation during 1998–2010. Journal of Geophysical Research: Space
- 638 *Physics*, 118(1), 232-243. https://doi.org/10.1029/2012JA017998
- Claudepierre, S. G., Mann, I. R., Takahashi, K., Fennell, J. F., Hudson, M. K., Blake, J. B., et al. (2013).
- Van Allen Probes observation of localized drift resonance between poloidal mode ultra-low
- frequency waves and 60 keV electrons. Geophys. Res. Lett., 40(17), 4491-4497.
- 642 https://doi.org/10.1002/grl.50901
- Dai, L., Takahashi, K., Lysak, R., Wang, C., Wygant, J. R., Kletzing, C., et al. (2015). Storm time
- occurrence and spatial distribution of Pc4 poloidal ULF waves in the inner magnetosphere: A
- Van Allen Probes statistical study. Journal of Geophysical Research: Space Physics, 120(6),
- 646 4748-4762. https://doi.org/10.1002/2015JA021134
- 647 Degeling, A. W., Rankin, R., Wang, Y., Shi, Q. Q., & Zong, Q. G. (2019). Alteration of Particle Drift
- Resonance Dynamics Near Poloidal Mode Field Line Resonance Structures. Journal of
- 649 Geophysical Research: Space Physics, 124(9), 7385-7401.
- 650 <u>https://doi.org/10.1029/2019JA026946</u>
- Elkington, S. R., Hudson, M. K., & Chan, A. A. (1999). Acceleration of relativistic electrons via drift-
- resonant interaction with toroidal-mode Pc-5 ULF oscillations. Geophysical Research Letters,
- 653 26(21), 3273-3276. https://doi.org/10.1029/1999GL003659
- Evans, D. S., & Greer, M. S. (2004). Polar orbiting environmental satellite space environment monitor-
- 2: instrument description and archive data documentation: NOAA Technical Memorandum 93,
- Version 1.4. Boulder, CO: Space Weather Predict. Cent.
- Fang, X., Randall, C. E., Lummerzheim, D., Wang, W., Lu, G., Solomon, S. C., & Frahm, R. A. (2010).
- Parameterization of monoenergetic electron impact ionization. Geophysical Research Letters,
- 659 37(22). https://doi.org/10.1029/2010GL045406
- 660 Fei, Y., Chan, A. A., Elkington, S. R., & Wiltberger, M. J. (2006). Radial diffusion and MHD particle
- simulations of relativistic electron transport by ULF waves in the September 1998 storm.

- 662 Journal of Geophysical Research: Space Physics, 111(A12).
 663 https://doi.org/10.1029/2005JA011211
- Foat, J. E., Lin, R. P., Smith, D. M., Fenrich, F., Millan, R., Roth, I., et al. (1998). First detection of a
 terrestrial MeV X-ray burst. Geophysical Research Letters, 25(22), 4109-4112.
 https://doi.org/10.1029/1998GL900134
- Foster, J. C., Wygant, J. R., Hudson, M. K., Boyd, A. J., Baker, D. N., Erickson, P. J., & Spence, H. E. (2015). Shock-induced prompt relativistic electron acceleration in the inner magnetosphere.

 Journal of Geophysical Research: Space Physics, 120(3), 1661-1674. https://doi.org/10.1002/2014JA020642
- Hamlin, D. A., Karplus, R., Vik, R. C., & Watson, K. M. (1961). Mirror and azimuthal drift frequencies
 for geomagnetically trapped particles. *J. Geophys. Res.*, 66(1), 1-4.
 https://doi.org/10.1029/JZ066i001p00001
- Hao, Y. X., Zong, Q.-G., Zhou, X.-Z., Rankin, R., Chen, X. R., Liu, Y., et al. (2017). Relativistic electron dynamics produced by azimuthally localized poloidal mode ULF waves: Boomerang-shaped pitch angle evolutions. *Geophys. Res. Lett.*, 44(15), 7618-7627. https://doi.org/10.1002/2017GL074006
- Horne, R. B., & Thorne, R. M. (2003). Relativistic electron acceleration and precipitation during resonant
 interactions with whistler-mode chorus. *Geophysical Research Letters*, 30(10).
 https://doi.org/10.1029/2003GL016973
- Hudson, M. K., Baker, D. N., Goldstein, J., Kress, B. T., Paral, J., Toffoletto, F. R., & Wiltberger, M.
 (2014). Simulated magnetopause losses and Van Allen Probe flux dropouts. *Geophysical Research Letters*, 41(4), 1113-1118. https://doi.org/10.1002/2014GL059222
- Hughes, W. J. (1994). Magnetospheric ULF Waves: A Tutorial with a Historical Perspective. In Solar
 Wind Sources of Magnetospheric Ultra Low Frequency Waves (pp. 1-11).
- Jaynes, A. N., Lessard, M. R., Takahashi, K., Ali, A. F., Malaspina, D. M., Michell, R. G., et al. (2015).

 Correlated Pc4–5 ULF waves, whistler-mode chorus, and pulsating aurora observed by the Van

 Allen Probes and ground-based systems. *Journal of Geophysical Research: Space Physics*,

 120(10), 8749-8761. https://doi.org/10.1002/2015JA021380
- Jordanova, V. K., Albert, J., & Miyoshi, Y. (2008). Relativistic electron precipitation by EMIC waves
 from self-consistent global simulations. J. Geophys. Res., 113(A3).
 https://doi.org/10.1029/2008JA013239
- Kataoka, R., & Miyoshi, Y. (2006). Flux enhancement of radiation belt electrons during geomagnetic storms driven by coronal mass ejections and corotating interaction regions. *Space Weather*, *4*(9). https://doi.org/10.1029/2005SW000211
- Kitamura, N., Kitahara, M., Shoji, M., Miyoshi, Y., Hasegawa, H., Nakamura, S., et al. (2018). Direct
 measurements of two-way wave-particle energy transfer in a collisionless space plasma. *Science*,
 361(6406), 1000-1003. https://doi.org/10.1126/science.aap8730
- Klimushkin, D. Y., Mager, P. N., Chelpanov, M. A., & Kostarev, D. V. (2021). Interaction between longperiod ULF waves and charged particle in the magnetosphere: theory and observations (overview). Solar-Terrestrial Physics, 7(4), 33-66. https://doi.org/10.12737/stp-74202105
- Kostarev, D. V., Mager, P. N., & Klimushkin, D. Y. (2021). Alfvén Wave Parallel Electric Field in the
 Dipole Model of the Magnetosphere: Gyrokinetic Treatment. Journal of Geophysical Research:
 Space Physics, 126(2), e2020JA028611. https://doi.org/10.1029/2020JA028611

- Lee, D.-H., and Lysak, R. L. (1989), Magnetospheric ULF wave coupling in the dipole model: The
- impulsive excitation, J. Geophys. Res., 94(A12), 17097– 17103.
- 707 https://doi.org/10.1029/JA094iA12p17097
- Lehtinen, N. G., Bell, T. F., and Inan, U. S. (1999), Monte Carlo simulation of runaway MeV electron
- breakdown with application to red sprites and terrestrial gamma ray flashes, J. Geophys. Res.,
- 710 104(A11), 24699–24712. https://doi.org/10.1029/1999JA900335
- 711 Li, L., Omura, Y., Zhou, X.-Z., Zong, Q.-G., Rankin, R., Yue, C., & Fu, S.-Y. (2022). Nonlinear Wave
- Growth Analysis of Chorus Emissions Modulated by ULF Waves. Geophysical Research
- 713 Letters, 49(10), e2022GL097978. https://doi.org/10.1029/2022GL097978
- Li, L., Zhou, X.-Z., Omura, Y., Zong, Q.-G., Rankin, R., Chen, X.-R., et al. (2021). Drift resonance
- between particles and compressional toroidal ULF waves in dipole magnetic field. Journal of
- 716 Geophysical Research: Space Physics, 126, e2020JA028842.
- 717 https://doi.org/10.1029/2020JA028842
- 718 Li, W., Mourenas, D., Artemyev, A. V., Agapitov, O. V., Bortnik, J., Albert, J. M., et al. (2014). Evidence
- of stronger pitch angle scattering loss caused by oblique whistler-mode waves as compared with
- quasi-parallel waves. Geophysical Research Letters, 41(17), 6063-6070.
- 721 https://doi.org/10.1002/2014GL061260
- Li, W., Ni, B., Thorne, R. M., Bortnik, J., Green, J. C., Kletzing, C. A., et al. (2013). Constructing the
- 723 global distribution of chorus wave intensity using measurements of electrons by the POES
- satellites and waves by the Van Allen Probes. *Geophysical Research Letters*, 40(17), 4526-4532.
- 725 https://doi.org/10.1002/grl.50920
- Li, W., Shen, X. C., Ma, Q., Capannolo, L., Shi, R., Redmon, R. J., et al. (2019). Quantification of
- Energetic Electron Precipitation Driven by Plume Whistler Mode Waves, Plasmaspheric Hiss,
- 728 and Exohiss. Geophysical Research Letters, 46(7), 3615-3624.
- 729 https://doi.org/10.1029/2019GL082095
- Li, W., Shprits, Y. Y., & Thorne, R. M. (2007). Dynamic evolution of energetic outer zone electrons due
- to wave-particle interactions during storms. Journal of Geophysical Research: Space Physics,
- 732 *112*(A10). https://doi.org/10.1029/2007JA012368
- 733 Li, W., Thorne, R. M., Bortnik, J., Nishimura, Y., & Angelopoulos, V. (2011). Modulation of whistler
- mode chorus waves: 1. Role of compressional Pc4–5 pulsations. *Journal of Geophysical*
- 735 Research: Space Physics, 116(A6). https://doi.org/10.1029/2010JA016312
- 736 Loto'aniu, T. M., Fraser, B. J., & Waters, C. L. (2009). The modulation of electromagnetic ion cyclotron
- 737 waves by Pc 5 ULF waves. Ann. Geophys., 27(1), 121-130. https://doi.org/10.5194/angeo-27-
- 738 121-2009
- Ma, Q., Connor, H. K., Zhang, X. J., Li, W., Shen, X. C., Gillespie, D., et al. (2020). Global Survey of
- 740 Plasma Sheet Electron Precipitation due to Whistler Mode Chorus Waves in Earth's
- 741 Magnetosphere. Geophysical Research Letters, 47(15), e2020GL088798.
- 742 https://doi.org/10.1029/2020GL088798
- Ma, Q., Li, W., Zhang, X. J., Bortnik, J., Shen, X. C., Connor, H. K., et al. (2021). Global Survey of
- 744 Electron Precipitation due to Hiss Waves in the Earth's Plasmasphere and Plumes. *Journal of*
- 745 Geophysical Research: Space Physics, 126(8), e2021JA029644.
- 746 https://doi.org/10.1029/2021JA029644

- Mann, I. R., Lee, E. A., Claudepierre, S. G., Fennell, J. F., Degeling, A., Rae, I. J., et al. (2013). Discovery
- of the action of a geophysical synchrotron in the Earth's Van Allen radiation belts. *Nature*
- 749 *Communications*, 4(1), 2795. https://doi.org/10.1038/ncomms3795
- 750 Marshall, R. A., & Bortnik, J. (2018). Pitch Angle Dependence of Energetic Electron Precipitation:
- Energy Deposition, Backscatter, and the Bounce Loss Cone. *Journal of Geophysical Research:*
- 752 *Space Physics, 123*(3), 2412-2423. https://doi.org/10.1002/2017JA024873
- 753 McPherron, R. L. (1979). Magnetospheric substorms. *Rev. Geophys.*, *17*(4), 657-681. 754 https://doi.org/10.1029/RG017i004p00657
- Meredith, N. P., Horne, R. B., Glauert, S. A., & Anderson, R. R. (2007). Slot region electron loss
- timescales due to plasmaspheric hiss and lightning-generated whistlers. *Journal of Geophysical*
- 757 Research: Space Physics, 112(A8). https://doi.org/10.1029/2007JA012413
- 758 Mikhailova, O. S., Smotrova, E. E., & Mager, P. N. (2022). Resonant Generation of an Alfvén Wave by
- a Substorm Injected Electron Cloud: A Van Allen Probe Case Study. Geophysical Research
- 760 Letters, 49(19), e2022GL100433. https://doi.org/10.1029/2022GL100433
- Millan, R. M., Lin, R. P., Smith, D. M., Lorentzen, K. R., & McCarthy, M. P. (2002). X-ray observations
- of MeV electron precipitation with a balloon-borne germanium spectrometer. Geophysical
- 763 Research Letters, 29(24), 47-41-47-44. https://doi.org/10.1029/2002GL015922
- Millan, R. M., Lin, R. P., Smith, D. M., & McCarthy, M. P. (2007). Observation of relativistic electron
- precipitation during a rapid decrease of trapped relativistic electron flux. Geophysical Research
- 766 Letters, 34(10). https://doi.org/10.1029/2006GL028653
- Millan, R. M., McCarthy, M. P., Sample, J. G., Smith, D. M., Thompson, L. D., McGaw, D. G., et al.
- 768 (2013). The Balloon Array for RBSP Relativistic Electron Losses (BARREL). Space Science
- 769 Reviews, 179(1), 503-530. https://doi.org/10.1007/s11214-013-9971-z
- 770 Millan, R. M., & Thorne, R. M. (2007). Review of radiation belt relativistic electron losses. *Journal of*
- 771 Atmospheric and Solar-Terrestrial Physics, 69(3), 362-377.
- 772 https://doi.org/10.1016/j.jastp.2006.06.019
- Murphy, K. R., Inglis, A. R., Sibeck, D. G., Watt, C. E. J., & Rae, I. J. (2020). Inner magnetospheric
- 774 ULF waves: The occurrence and distribution of broadband and discrete wave activity. Journal
- 775 of Geophysical Research: Space Physics, 125, e2020JA027887.
- 776 https://doi.org/10.1029/2020JA027887
- Ni, B., Bortnik, J., Nishimura, Y., Thorne, R. M., Li, W., Angelopoulos, V., et al. (2014). Chorus wave
- 778 scattering responsible for the Earth's dayside diffuse auroral precipitation: A detailed case study.
- 779 Journal of Geophysical Research: Space Physics, 119(2), 897-908.
- 780 https://doi.org/10.1002/2013JA019507
- Ni, B., Bortnik, J., Thorne, R. M., Ma, Q., & Chen, L. (2013). Resonant scattering and resultant pitch
- angle evolution of relativistic electrons by plasmaspheric hiss. *Journal of Geophysical Research*:
- 783 Space Physics, 118(12), 7740-7751. https://doi.org/10.1002/2013JA019260
- Ni, B., Thorne, R. M., Shprits, Y. Y., & Bortnik, J. (2008). Resonant scattering of plasma sheet electrons
- by whistler-mode chorus: Contribution to diffuse auroral precipitation. *Geophysical Research*
- 786 Letters, 35(11). https://doi.org/10.1029/2008GL034032
- 787 Nishimura, Y., Bortnik, J., Li, W., Thorne, R. M., Lyons, L. R., Angelopoulos, V., et al. (2010).
- 788 Identifying the driver of pulsating aurora. science, 330(6000), 81-84.
- 789 https://doi.org/10.1126/science.1193186

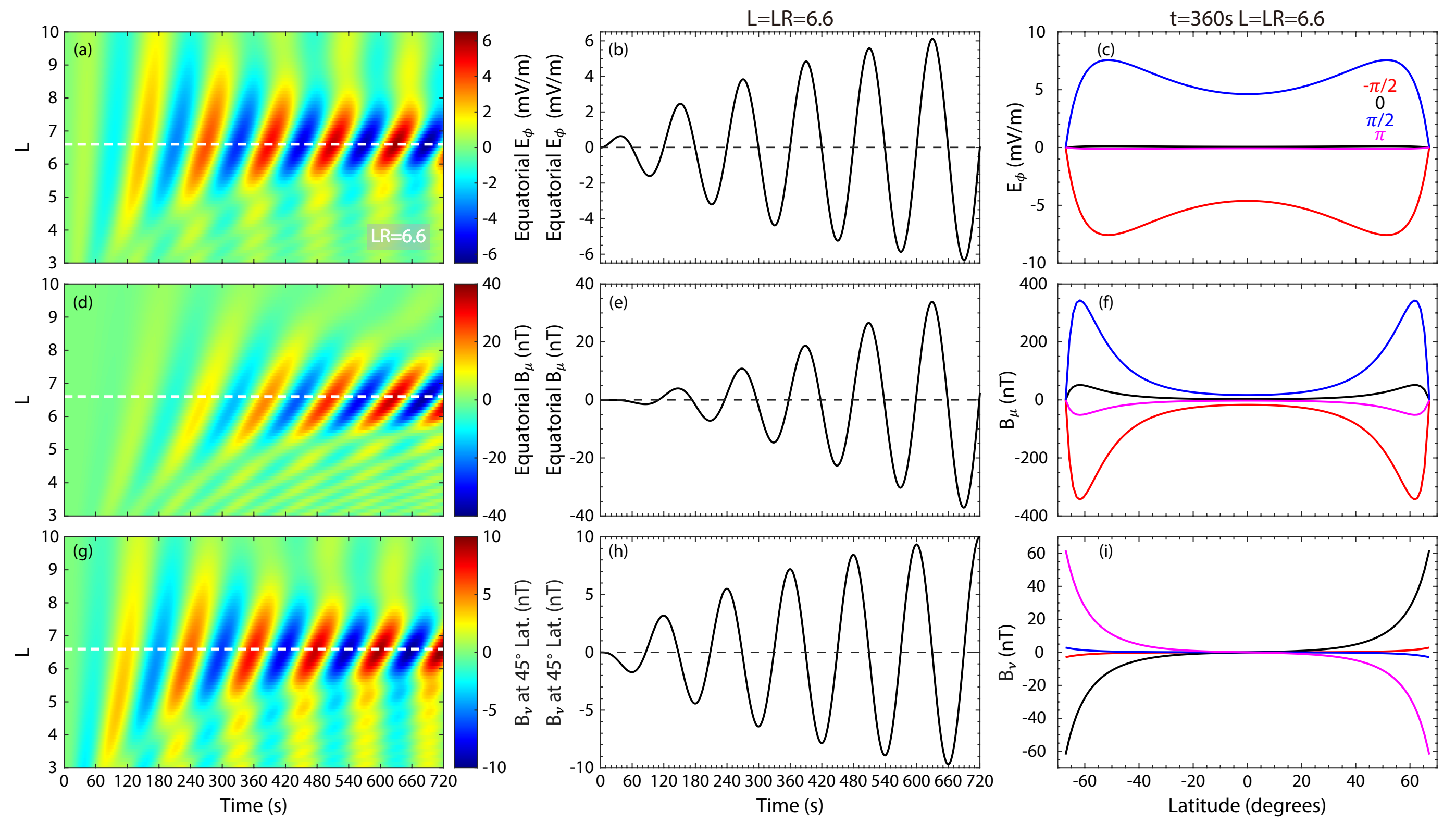
- 790 Northrop, T. G. (1963). Adiabatic charged-particle motion. *Rev. Geophys.*, 1(3), 283-304. 791 https://doi.org/10.1029/RG001i003p00283
- Omura, Y., Pickett, J., Grison, B., Santolik, O., Dandouras, I., Engebretson, M., et al. (2010). Theory and observation of electromagnetic ion cyclotron triggered emissions in the magnetosphere. *Journal of Geophysical Research: Space Physics*, 115(A7). https://doi.org/10.1029/2010JA015300
- Posch, J. L., Engebretson, M. J., Pilipenko, V. A., Hughes, W. J., Russell, C. T., and Lanzerotti, L. J.
 (2003), Characterizing the long-period ULF response to magnetic storms. J. Geophys. Res.,
 108(A1). https://doi.org/10.1029/2002JA009386
- Qin, M., Li, W., Ma, Q., Woodger, L., Millan, R., Shen, X.-C., & Capannolo, L. (2021). Multi-point observations of modulated whistler-mode waves and energetic electron precipitation. Journal of Geophysical Research: Space Physics, 126, e2021JA029505. https://doi.org/10.1029/2021JA029505
- Rae, I. J., Murphy, K. R., Watt, C. E. J., Halford, A. J., Mann, I. R., Ozeke, L. G., et al. (2018). The Role of Localized Compressional Ultra-low Frequency Waves in Energetic Electron Precipitation.

 Journal of Geophysical Research: Space Physics, 123(3), 1900-1914. https://doi.org/10.1002/2017JA024674
- Randall, C. E., Harvey, V. L., Singleton, C. S., Bailey, S. M., Bernath, P. F., Codrescu, M., et al. (2007).
 Energetic particle precipitation effects on the Southern Hemisphere stratosphere in 1992–2005.
 Journal of Geophysical Research: Atmospheres, 112(D8).
 https://doi.org/10.1029/2006JD007696
- Rankin, R., Gillies, D. M., & Degeling, A. W. (2021). On the Relationship Between Shear Alfvén Waves,
 Auroral Electron Acceleration, and Field Line Resonances. Space Science Reviews, 217(4), 60.
 https://doi.org/10.1007/s11214-021-00830-x
- Rankin, R., Kabin, K., Lu, J. Y., Mann, I. R., Marchand, R., Rae, I. J., et al. (2005). Magnetospheric field-line resonances: Ground-based observations and modeling. *Journal of Geophysical Research: Space Physics, 110*(A10). https://doi.org/10.1029/2004JA010919
- Rankin, R., Samson, J. C., Tikhonchuk, V. T., & Voronkov, I. (1999). Auroral density fluctuations on dispersive field line resonances. *J. Geophys. Res.*, 104(A3), 4399-4410.
 https://doi.org/10.1029/1998JA900106
- Rodger, C. J., Clilverd, M. A., Green, J. C., & Lam, M. M. (2010). Use of POES SEM-2 observations to examine radiation belt dynamics and energetic electron precipitation into the atmosphere.
- 821 *Journal of Geophysical Research: Space Physics, 115*(A4). 822 https://doi.org/10.1029/2008JA014023. https://doi.org/10.1029/2008JA014023
- Shprits, Y. Y., Meredith, N. P., & Thorne, R. M. (2007). Parameterization of radiation belt electron loss timescales due to interactions with chorus waves. *Geophysical Research Letters*, *34*(11). https://doi.org/10.1029/2006GL029050
- Shprits, Y. Y., Thorne, R. M., Friedel, R., Reeves, G. D., Fennell, J., Baker, D. N., & Kanekal, S. G. (2006). Outward radial diffusion driven by losses at magnetopause. *Journal of Geophysical Research: Space Physics, 111*(A11). https://doi.org/10.1029/2006JA011657
- Sinnhuber, M., & Funke, B. (2020). Chapter 9 Energetic electron precipitation into the atmosphere. In
 A. N. Jaynes & M. E. Usanova (Eds.), *The Dynamic Loss of Earth's Radiation Belts* (pp. 279321): Elsevier.

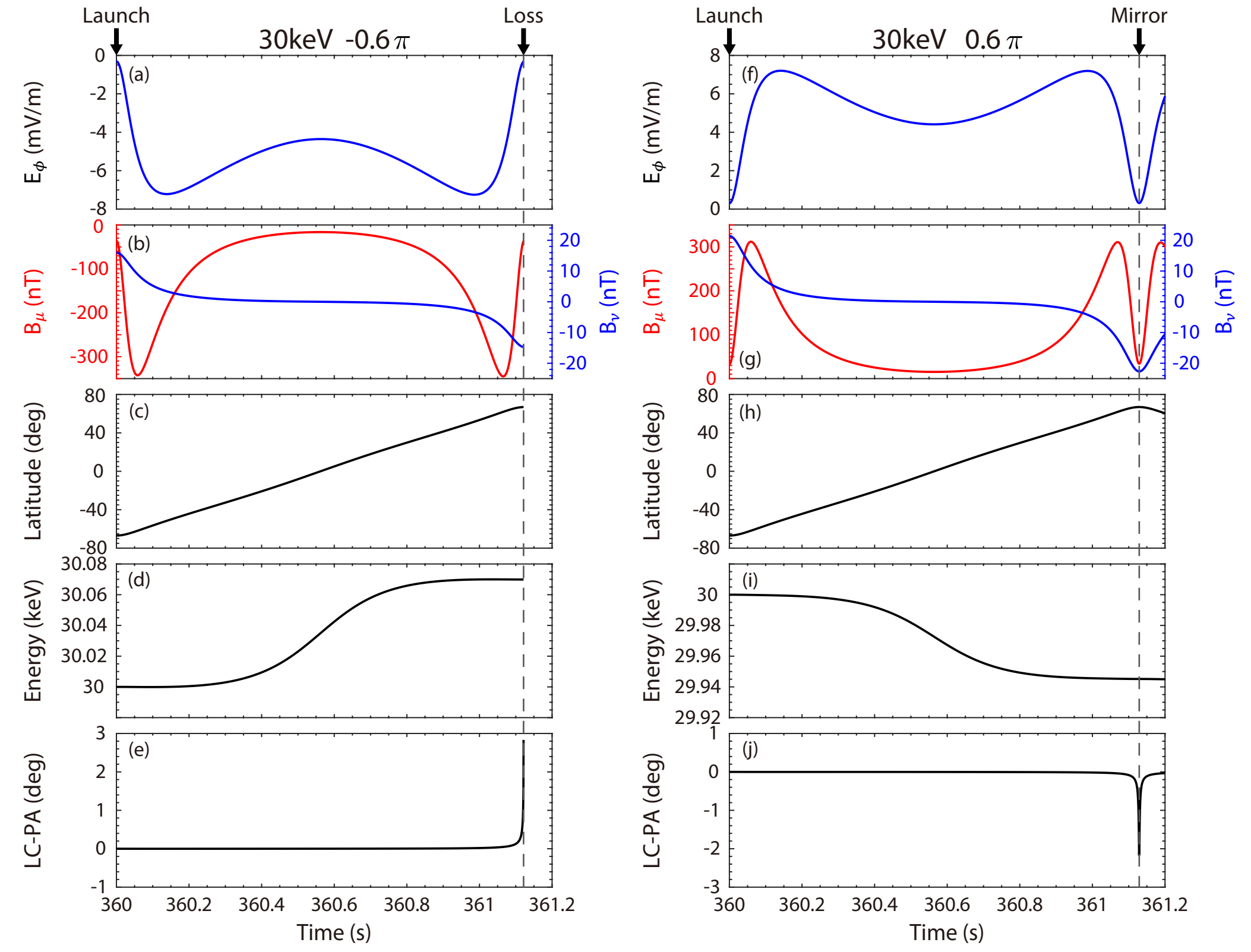
- 832 Southwood, D. J., & Kivelson, M. G. (1981). Charged particle behavior in low-frequency geomagnetic
- pulsations 1. Transverse waves. J. Geophys. Res., 86(A7), 5643-5655.
- https://doi.org/10.1029/JA086iA07p05643
- 835 Southwood, D. J., & Kivelson, M. G. (1982). Charged particle behavior in low-frequency geomagnetic
- pulsations, 2. Graphical approach. J. Geophys. Res., 87(A3), 1707-1710.
- 837 https://doi.org/10.1029/JA087iA03p01707
- 838 Su, Z., Zhu, H., Xiao, F., Zong, Q. G., Zhou, X. Z., Zheng, H., et al. (2015). Ultra-low-frequency wave-
- driven diffusion of radiation belt relativistic electrons. *Nature Communications*, 6(1), 10096.
- 840 https://doi.org/10.1038/ncomms10096
- Thorne, R. M., and Kennel, C. F. (1971), Relativistic electron precipitation during magnetic storm main
- phase, J. Geophys. Res., 76(19), 4446–4453. https://doi.org/10.1029/JA076i019p04446
- Thorne, R. M., Ni, B., Tao, X., Horne, R. B., & Meredith, N. P. (2010). Scattering by chorus waves as
- the dominant cause of diffuse auroral precipitation. *Nature*, 467(7318), 943-946.
- 845 https://doi.org/10.1038/nature09467
- Ukhorskiy, A. Y., Anderson, B. J., Brandt, P. C., & Tsyganenko, N. A. (2006). Storm time evolution of
- the outer radiation belt: Transport and losses. Journal of Geophysical Research: Space Physics,
- 848 *111*(A11). https://doi.org/10.1029/2006JA011690
- Usanova, M. E., Drozdov, A., Orlova, K., Mann, I. R., Shprits, Y., Robertson, M. T., et al. (2014). Effect
- of EMIC waves on relativistic and ultrarelativistic electron populations: Ground-based and Van
- Allen Probes observations. Geophys. Res. Lett., 41(5), 1375-1381.
- https://doi.org/10.1002/2013GL059024
- Vette, J. I. (1991). The AE-8 trapped electron model environment (Vol. 91, No. 24): National Space
- Science Data Center (NSSDC), World Data Center A for Rockets and Satellites (WDC-AR &S),
- National Aeronautics and Space Administration, Goddard Space Flight Center.
- Wang, C., Rankin, R., Wang, Y., Zong, Q. G., Zhou, X., Takahashi, K., et al. (2018). Poloidal Mode
- 857 Wave-Particle Interactions Inferred From Van Allen Probes and CARISMA Ground-Based
- Observations. Journal of Geophysical Research: Space Physics, 123(6), 4652-4667.
- 859 https://doi.org/10.1029/2017JA025123
- 860 Wright, A. N., & Elsden, T. (2020). Simulations of MHD wave propagation and coupling in a 3-D
- 861 magnetosphere. Journal of Geophysical Research: Space Physics, 125, e2019JA027589.
- 862 https://doi.org/10.1029/2019JA027589
- 863 Xia, Z., Chen, L., Dai, L., Claudepierre, S. G., Chan, A. A., Soto-Chavez, A. R., & Reeves, G. D. (2016).
- 864 Modulation of chorus intensity by ULF waves deep in the inner magnetosphere. *Geophysical*
- Research Letters, 43(18), 9444-9452. https://doi.org/10.1002/2016gl070280
- Xu, W., Marshall, R. A., Fang, X., Turunen, E., & Kero, A. (2018). On the Effects of Bremsstrahlung
- Radiation During Energetic Electron Precipitation. *Geophysical Research Letters*, 45(2), 1167-
- 868 1176. https://doi.org/10.1002/2017GL076510
- 869 Yin, Z., Zou, H., Ye, Y., Zong, Q., & Wang, Y. (2019). Superposed Epoch Analysis of the Energetic
- 870 Electron Flux Variations During CIRs Measured by BD-IES. Space Weather, 17(12), 1765-
- 871 1782. https://doi.org/10.1029/2019SW002296
- 872 Zhang, X.-J., Chen, L., Artemyev, A. V., Angelopoulos, V., & Liu, X. (2019). Periodic Excitation of
- Chorus and ECH Waves Modulated by Ultralow Frequency Compressions. J. Geophys. Res.
- 874 Space Physics, 124(11), 8535-8550. https://doi.org/10.1029/2019ja027201

- Zhang, X. J., Mourenas, D., Artemyev, A. V., Angelopoulos, V., & Sauvaud, J. A. (2019). Precipitation
 of MeV and Sub-MeV Electrons Due to Combined Effects of EMIC and ULF Waves. *Journal* of Geophysical Research: Space Physics, 124(10), 7923-7935.
 https://doi.org/10.1029/2019JA026566
- Zhou, X.-Z., Wang, Z.-H., Zong, Q.-G., Claudepierre, S. G., Mann, I. R., Kivelson, M. G., et al. (2015),
 Imprints of impulse-excited hydromagnetic waves on electrons in the Van Allen radiation belts,
 Geophysical Research Letters, 42(15), 6199-6204. https://doi.org/10.1002/2015GL064988
- Zhou, X.-Z., Wang, Z.-H., Zong, Q.-G., Rankin, R., Kivelson, M. G., Chen, X.-R., et al. (2016). Charged particle behavior in the growth and damping stages of ultralow frequency waves: Theory and Van Allen Probes observations. *Journal of Geophysical Research: Space Physics, 121*(4), 3254-3263. https://doi.org/10.1002/2016JA022447
- Zong, Q. G., Rankin, R., & Zhou, X. (2017). The interaction of ultra-low-frequency pc3-5 waves with charged particles in Earth's magnetosphere. *Reviews of Modern Plasma Physics, 1*(1), 1-90. https://doi.org/10.1007/s41614-017-0011-4
- Zong, Q. G., Wang, Y., Yuan, C., Yang, B., Wang, C., & Zhang, X. (2011). Fast acceleration of "killer" electrons and energetic ions by interplanetary shock stimulated ULF waves in the inner magnetosphere. *Chinese science bulletin*, 56(12), 1188. https://doi.org/10.1007/s11434-010-4308-8
- Zong, Q. G., Zhou, X. Z., Wang, Y. F., Li, X., Song, P., Baker, D. N., et al. (2009). Energetic electron response to ULF waves induced by interplanetary shocks in the outer radiation belt. *Journal of Geophysical Research: Space Physics*, 114(A10). https://doi.org/10.1029/2009JA014393

| Figure | 1. |
|--------|----|
|--------|----|



| Figure | 2. |
|--------|----|
|--------|----|



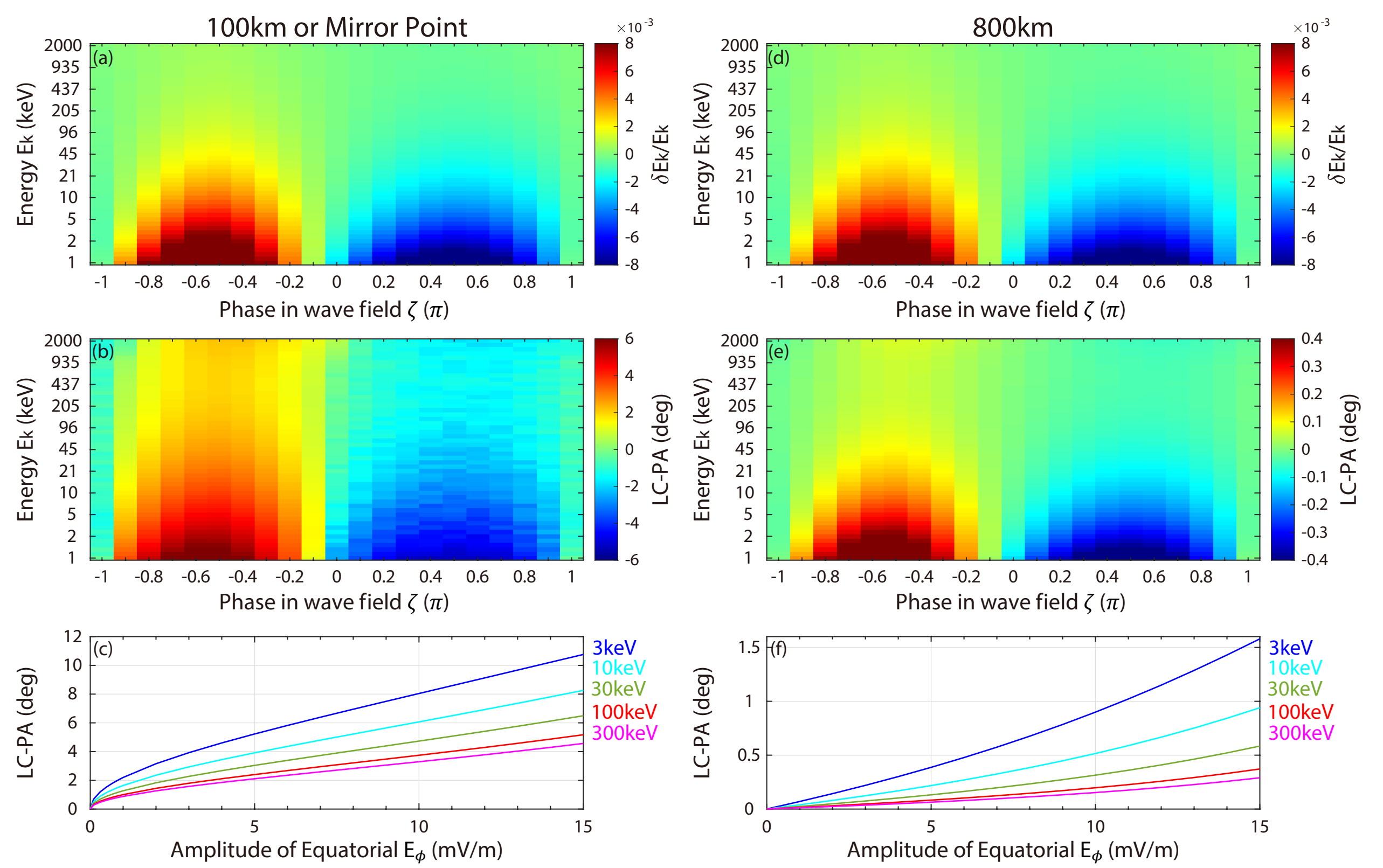


| Figure 4. | |
|-----------|--|
|-----------|--|

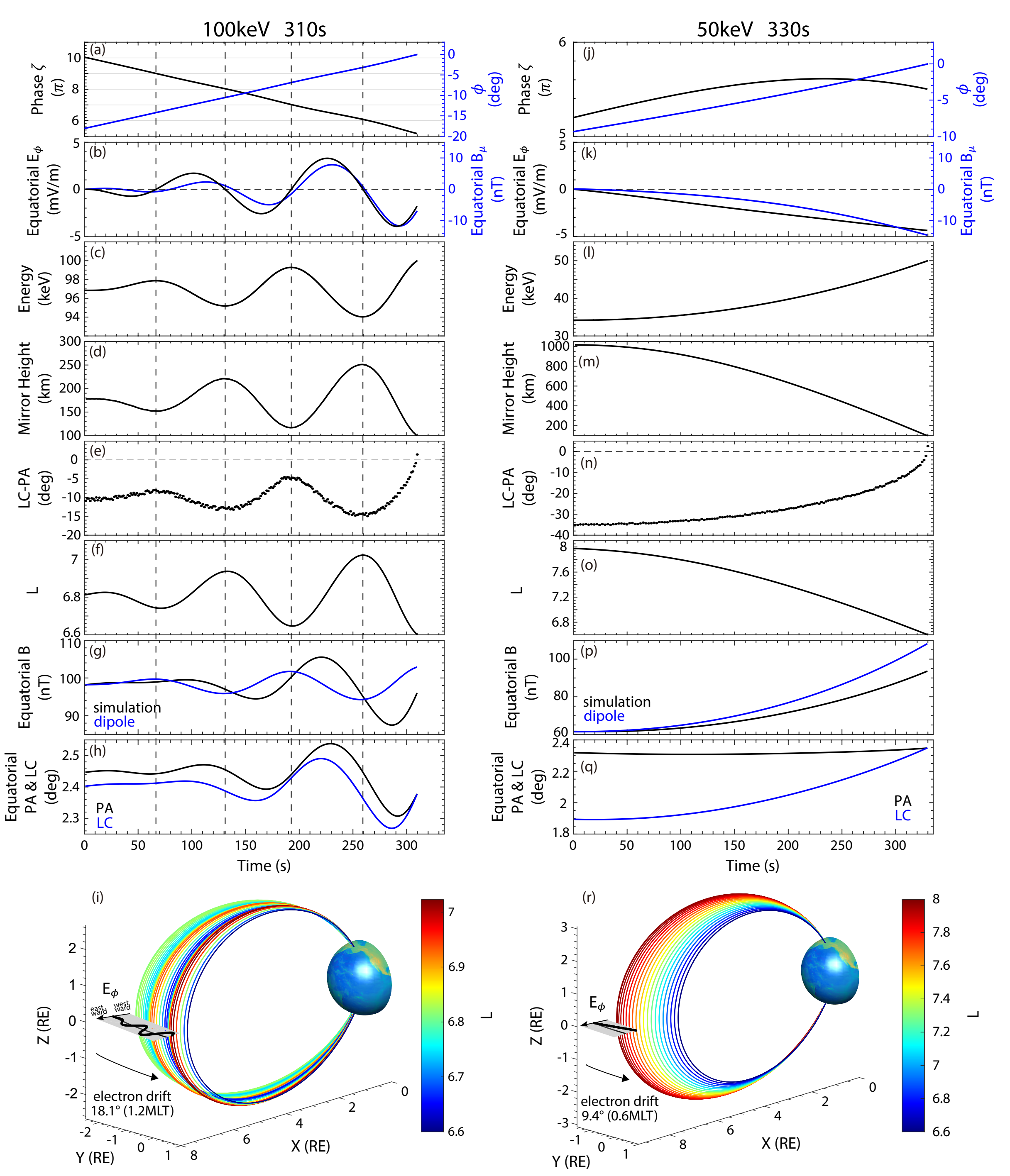


| Figure 5. | |
|-----------|--|
|-----------|--|

